

Fast Asymmetric Fronts Propagation for Voronoi Region Partitioning and Image Segmentation

Da Chen and Laurent D. Cohen

CEREMADE, CNRS,
University Paris Dauphine, PSL Research University,
UMR 7534, 75016 PARIS, FRANCE

Abstract. In this paper, we introduce a generalized asymmetric fronts propagation model based on the geodesic distance maps and the Eikonal partial differential equations. One of the key ingredients for the computation of the geodesic distance map is the geodesic metric, which can govern the action of the geodesic distance level set propagation. We consider a Finsler metric with the Randers form, through which the asymmetry and anisotropy enhancements can be taken into account to prevent the fronts leaking problem during the fronts propagation. These enhancements can be derived from the image edge-dependent vector field such as the gradient vector flow. The numerical implementations are carried out by the Finsler variant of the fast marching method, leading to very efficient interactive segmentation schemes.

1 Introduction

Fronts propagation models have been considerably developed since the original level set framework proposed by Osher and Sethian [1]. Guaranteed by the solid mathematical background, the fronts propagation models lead to strong abilities in a wide variety of computer vision tasks such as image segmentation [2–5]. In their basic formulation, the boundaries of an object are modelled as closed contours, each of which can be obtained by evolving an initial closed curve till the stopping criteria are reached. The use of curve evolution scheme for image segmentation can be back-track to the original active contour model [6].

Let $\Omega \subset \mathbb{R}^2$ be an open bounded domain. Based on the level set framework [1], a closed contour γ can be retrieved by identifying the zero level set line of a function $\phi : \Omega \rightarrow \mathbb{R}$ such that $\gamma := \{\mathbf{x} \in \Omega; \phi(\mathbf{x}) = 0\}$. By this curve representation, the curve evolution is carried out by evolving the function ϕ

$$\partial\phi/\partial t = \xi \|\nabla\phi\|, \quad (1)$$

where $\xi : \Omega \rightarrow \mathbb{R}$ is a speed function and t denotes the time. At any time t , the curve γ can be recovered by identifying the zero-level set lines of ϕ . Using the level set evolutionary equation (1), the contours splitting and merging can be adaptively handled. The main drawback of the level set-based front propagation method is its expensive computational burden. In order to alleviate this

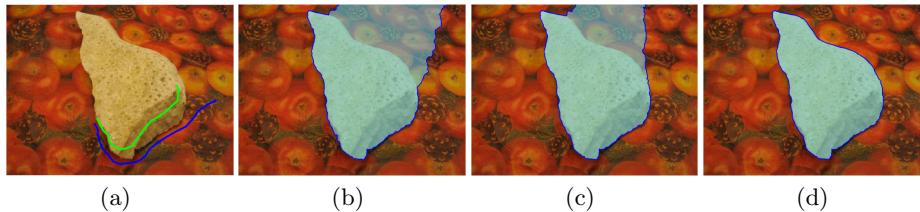


Fig. 1. Image segmentation through different metrics. **a** The original image and seeds. **b-d** Segmentation results via isotropic Riemannian metric, anisotropic Riemannian metric and the proposed Finsler metric.

problem, Adalsteinsson and Sethian [7] suggested to restrict the computation for the update of the level set function ϕ within a narrow band such that only the values of ϕ at the points within this narrowband are updated according to Eq. (1). Moreover, the distance-preserving level set method [8] is able to avoid level set reinitialization by enforcing the level set function ϕ as a signed Euclidean distance function from the current curves during the evolution.

Despite the efforts devoted to the reduction of the computation burden, the classical level set-based fronts propagation scheme (1) is still impractical especially for realtime applications. In order to solve this issue, Malladi and Sethian [9] proposed a new geodesic distance-based fronts propagation model for real time image segmentation. It relies on a geodesic distance map $\mathcal{U}_{\mathfrak{s}} : \Omega \rightarrow \mathbb{R}^+ \cup \{0\}$ associated to a collection $\mathfrak{s} \subset \Omega$ of source points. The value of $\mathcal{U}_{\mathfrak{s}}(\mathbf{x})$ in essence equals to the minimal geodesic length between \mathbf{x} and a source point $\mathfrak{s} \in \mathfrak{s}$ associated to an isotropic Riemannian metric. The numerical computation of $\mathcal{U}_{\mathfrak{s}}$ can be carried out by the fast marching method [10, 11]. The efficiency of the fast marching methods provide the possibility of real time segmentation application. Based on the geodesic distance map $\mathcal{U}_{\mathfrak{s}}$, a curve can be denoted by the T -level set of $\mathcal{U}_{\mathfrak{s}}$, where $T > 0$ is a geodesic distance thresholding value. In other words, a curve γ can be characterized at the distance value T such that

$$\gamma := \{\mathbf{x} \in \Omega; \mathcal{U}_{\mathfrak{s}}(\mathbf{x}) = T\}. \quad (2)$$

One difficulty suffered by the geodesic distance-based fronts propagation scheme is that the fronts may leak outside the targeted regions before all the points of these regions have been visited by the fronts. The leaking problem sometimes occurs near the boundaries close to the source positions or in weak boundaries, especially when handling long and thin structures. The main reason for this leaking problem is the positivity constraint required by the Eikonal equation. Chen and Cohen [12] considered an anisotropic Riemannian metric for fronts propagation, where the path orientations are taken into account to mitigate the leaking problem. Arbelaez and Cohen [13] and Bai and Sapiro [14] made use of the concept of Voronoi index map which is constructed by the geodesic distance associated to the orientation-dependent pseudo path metric, the values of which are allowed to be zero. The image segmentation can be characterized

by the Voronoi regions, each of which involves all the points with the same voronoi index. In this case, the contours indicating the tagged object edges are common boundaries of the adjacent voronoi regions. Li and Yezzi [15] proposed a dual fronts propagation model for active contours evolution, where the geodesic metric comprises both edge and region statistical information. The basic idea of [15] is to propagate the fronts simultaneously from the exterior and interior boundaries of the narrowband. The optimal contours can be recovered from the positions where the two fast marching fronts meet. These meeting interfaces also correspond to the boundaries of the adjacent voronoi regions.

In this paper we extend the geodesic distance-based fronts propagation framework to the Finsler case, where the edge anisotropy and asymmetry are taken into account simultaneously. Moreover, we present a way to construct the Finsler metric with respect to foreground and background segmentation. The existing fronts propagation methods invoking either Riemannian metric [12, 16] or pseudo path metric [13, 14], do not take into account the edge asymmetry information. This may lead to leaking problem when the seeds are close to the targeted boundaries. We show an example of such problems in Fig. 1, where the seeds are shown in Fig. 1a with green and red brushes indicating background and foreground. It can be seen that the segmentation contours from the Riemannian metrics shown in Figs. 1b and 1c cross the boundaries before the whole object has been covered by the fronts. In contrast, the segmentation results from the proposed Finsler metric case can catch the desired boundary (see Fig. 1d).

1.1 Paper Outline

The remaining of this paper is organized as follows: In Section 2, we introduce the geodesic distance map associated to a general Finsler metric, the Voronoi regions and the relevant numerical tool. Section 3 presents construction principle for the asymmetric Finsler metric. The numerical considerations for the Finsler metric-based fronts propagation are introduced in Section 4. The experimental results and the conclusion are respectively presented in Sections 5 and 6.

2 Background on Geodesic Distance Map

A Finsler geodesic metric $\mathcal{F} : \Omega \times \mathbb{R}^2 \rightarrow [0, +\infty]$ is a continuous function over the domain $\Omega \times \mathbb{R}^2$. For each fixed point $\mathbf{x} \in \Omega$, the geodesic metric $\mathcal{F}(\mathbf{x}, \mathbf{v})$ can be characterized by an asymmetric norm of $\mathbf{v} \in \mathbb{R}^2$. In other words, \mathcal{F} is convex and 1-homogeneous on its second argument. It is also potentially asymmetric such that $\exists \mathbf{x} \in \Omega$ and $\exists \mathbf{v} \in \mathbb{R}^2$, the inequality $\mathcal{F}(\mathbf{x}, \mathbf{v}) \neq \mathcal{F}(\mathbf{x}, -\mathbf{v})$ is held.

The curve length associated to the metric \mathcal{F} along a Lipschitz continuous curve \mathcal{C} can be expressed by $\ell_{\mathcal{F}}(\mathcal{C}) := \int_{\mathcal{C}} \mathcal{F}(\mathcal{C}(s), \mathcal{C}'(s)) ds$ with s the arc-length parameter of \mathcal{C} . It is possible for the geodesic length $\ell_{\mathcal{F}}$ to take into account both the path directions and image data [17]. Letting $\mathfrak{s} \subset \Omega$ be the set of the source points, the minimal curve length from \mathbf{y} to \mathbf{x} associated to the metric \mathcal{F}

is defined by

$$\mathcal{D}_{\mathcal{F}}(\mathbf{y}, \mathbf{x}) = \inf_{\mathcal{C} \in \mathcal{A}_{\mathbf{y}, \mathbf{x}}} \ell_{\mathcal{F}}(\mathcal{C}), \quad (3)$$

where $\mathcal{A}_{\mathbf{y}, \mathbf{x}}$ is the set of Lipschitz continuous curves linking \mathbf{y} to $\mathbf{x} \in \Omega$. The geodesic distance map $\mathcal{U}_{\mathfrak{s}}$ associated to the metric \mathcal{F} can be defined by

$$\mathcal{U}_{\mathfrak{s}}(\mathbf{x}) := \inf_{\mathfrak{s} \in \mathfrak{s}} \mathcal{D}_{\mathcal{F}}(\mathfrak{s}, \mathbf{x}), \quad (4)$$

It is the unique viscosity solution to the Eikonal equation such that $\mathcal{U}_{\mathfrak{s}}(\mathbf{x}) = 0$, $\forall \mathbf{x} \in \mathfrak{s}$, and

$$\max_{\|\mathbf{v}\| \neq 0} \frac{\langle \nabla \mathcal{U}_{\mathfrak{s}}(\mathbf{x}), \mathbf{v} \rangle}{\mathcal{F}(\mathbf{x}, \mathbf{v})} = 1, \quad \forall \mathbf{x} \in \Omega \setminus \mathfrak{s}, \quad (5)$$

where $\nabla \mathcal{U}_{\mathfrak{s}}(\cdot)$ denote the Euclidean gradient vector and $\langle \cdot, \cdot \rangle$ is the standard Euclidean scalar product in \mathbb{R}^2 . The Eikonal equation (5) can be interpreted by the Bellman's optimality principle such that

$$\mathcal{U}_{\mathfrak{s}}(\mathbf{x}) = \min_{\mathbf{y} \in \partial \Lambda(\mathbf{x})} \{\mathcal{D}_{\mathcal{F}}(\mathbf{y}, \mathbf{x}) + \mathcal{U}_{\mathfrak{s}}(\mathbf{y})\}, \quad (6)$$

where $\Lambda(\mathbf{x})$ is a neighbourhood of point \mathbf{x} and $\partial \Lambda(\mathbf{x})$ is the boundary of $\Lambda(\mathbf{x})$.

2.1 Voronoi Index Map

We consider a more general case for which a family of source point sets, denoted by \mathfrak{s}_k , are provided. These sets are indexed by $k \in \{1, 2, \dots, n\}$ with n the total number of source point sets. For the sake of simplicity, we note $\mathfrak{s} = \cup_{k=1}^n \mathfrak{s}_k$. A Voronoi index map can be defined as a labelling function $\mathcal{L} : \Omega \rightarrow \{1, 2, 3, \dots, n\}$, which satisfies that $\mathcal{L}(\mathbf{x}) = k$, $\forall \mathbf{x} \in \mathfrak{s}_k$. In the sense of the geodesic distance \mathcal{U}_k , the Voronoi index map \mathcal{L} assigns a label identical to the index of its closest source point set such that

$$\mathcal{L}(\mathbf{x}) = \arg \min_{1 \leq k \leq n} \mathcal{U}_k(\mathbf{x}). \quad (7)$$

By the map \mathcal{L} , one can partition the domain Ω into n Voronoi regions $\mathcal{V}_k \subset \Omega$

$$\mathcal{V}_k := \{\mathbf{x} \in \Omega; \mathcal{L}(\mathbf{x}) = k\}. \quad (8)$$

The common boundary $\Gamma_{i,j} := \partial \mathcal{V}_i \cap \partial \mathcal{V}_j$ of two adjacent voronoi regions \mathcal{V}_i and \mathcal{V}_j is comprised of a set of equidistant points to the collections \mathfrak{s}_i and \mathfrak{s}_j . The geodesic distance map $\mathcal{U}_{\mathfrak{s}}$ associated to $\mathfrak{s} = \cup_k \mathfrak{s}_k$ can be computed by

$$\mathcal{U}_{\mathfrak{s}}(\mathbf{x}) = \min_{1 \leq k \leq n} \mathcal{U}_k(\mathbf{x}). \quad (9)$$

2.2 Fast Marching Method

The fast marching method is a very efficient way to estimate the geodesic distance map. One key point of the fast marching method is the stencil map Λ , where $\Lambda(\mathbf{x})$ defines the neighbourhood of a grid point \mathbf{x} . The original fast marching methods [10, 11] are established on the regular 4-connectivity neighbourhood system, which may suffer some difficulties for the general Finsler metric. Alternatively, the Finsler variant of the fast marching method [18] make use of a complicated neighbourhood system depending on the metric.

The Finsler invariant of the fast marching method [18] estimates the distance values on a discretization grid \mathbb{Z}^2 of the domain Ω . It makes use of the Hopf-Lax operator to approximate the Eikonal equation (6) such that

$$\mathcal{U}_s(\mathbf{x}) = \min_{\mathbf{y} \in \partial\Lambda(\mathbf{x})} \{\mathcal{F}(\mathbf{x}, \mathbf{x} - \mathbf{y}) + \mathbb{I}_{\Lambda(\mathbf{x})} \mathcal{U}_s(\mathbf{y})\}, \quad (10)$$

where $\Lambda(\mathbf{x})$ denotes the stencil of \mathbf{x} involving a set of vertices in \mathbb{Z}^2 and $\mathbb{I}_{\Lambda(\mathbf{x})}$ is a piecewise linear interpolation operator in the neighbourhood $\Lambda(\mathbf{x})$. The minimal curve length $\mathcal{D}_{\mathcal{F}}$ of a short geodesic from \mathbf{y} to \mathbf{x} is approximated by the value of $\mathcal{F}(\mathbf{x}, \mathbf{x} - \mathbf{y})$. The distance value $\mathcal{U}_s(\mathbf{y})$ in Eq. (6) is estimated by the piecewise linear interpolation operator $\mathbb{I}_{\Lambda(\mathbf{x})}$ at \mathbf{y} located at the stencil boundary $\partial\Lambda(\mathbf{x})$. It is comprised of a set $\mathcal{T}_{\mathbf{x}}$ of 1-dimensional simplexes or line segments. Each simplex $\mathbb{T}_i \in \mathcal{T}_{\mathbf{x}}$ connects two adjacent vertices which are involved in the stencil $\Lambda(\mathbf{x})$. The solution \mathcal{U}_s to the Hopf-Lax operator (10) can be attained by

$$\mathcal{U}_s(\mathbf{x}) = \min_{\mathbb{T}_i \in \mathcal{T}_{\mathbf{x}}} U_i(\mathbf{x}), \quad (11)$$

where U_i is the solution to the minimization problem

$$U_i(\mathbf{x}) = \min_{\mathbf{y} \in \mathbb{T}_i} \{\mathcal{F}(\mathbf{x}, \mathbf{x} - \mathbf{y}) + \mathbb{I}_{\Lambda(\mathbf{x})} \mathcal{U}_s(\mathbf{y})\}. \quad (12)$$

For each simplex $\mathbb{T}_i \in \mathcal{T}_{\mathbf{x}}$ which joins two vertices \mathbf{z}_1 and \mathbf{z}_2 , the minimization problem (12) can be approximated by Tsitsiklis' theorem [11] such that

$$U_i(\mathbf{x}) = \min_{\boldsymbol{\lambda}} \mathcal{F} \left(\mathbf{x}, \mathbf{x} - \sum_{i=1}^2 \lambda_i \mathbf{z}_i \right) + \sum_{i=1}^2 \lambda_i \mathcal{U}_s(\mathbf{z}_i), \quad (13)$$

where $\boldsymbol{\lambda} = (\lambda_1, \lambda_2)$ subject to $\lambda_1, \lambda_2 \geq 0$ and $\sum_i^2 \lambda_i = 1$.

Fast Marching Update Scheme. The fast marching method estimates the geodesic distance map \mathcal{U}_s in a wave front propagation manner. The fast marching fronts propagation is coupled with a procedure of label assignment operation, during which all the grid points are classified into three categories: *Accepted* points (for which the values of \mathcal{U}_s have been estimated and frozen), *Far* points (for which the values of \mathcal{U}_s are unknown), and *Trial* points (the remaining grid points in \mathbb{Z}^2 which form the fast marching *fronts*). A *Trial* point will be assigned a label of *Accepted* if it has the minimal geodesic distance value among

all the *Trial* points. In the course of the geodesic distance estimation, each grid point $\mathbf{x} \in \mathbb{Z}^2 \setminus \mathfrak{s}$ will be visited by the monotonically advancing fronts which expand from the source points involved in \mathfrak{s} . The values of $\mathcal{U}_{\mathfrak{s}}$ for all the *Trial* points are stored in a priority queue in order to quickly find the point with minimal $\mathcal{U}_{\mathfrak{s}}$. The label assignment procedure¹ can be carried out by a binary map $b : \mathbb{Z}^2 \rightarrow \{\textit{Accepted}, \textit{Far}, \textit{Trial}\}$.

Suppose that $\mathfrak{s} = \cup_k \mathfrak{s}_k$ with \mathfrak{s}_k a source point set. The geodesic distance map $\mathcal{U}_{\mathfrak{s}}$ and the Voronoi index map \mathcal{L} can be simultaneously computed [19, 20], where the computation scheme in each iteration can be divided into two steps.

Voronoi index update. In each geodesic distance update iteration, among all the *Trial* points, a point \mathbf{x}_{\min} that globally minimizes the geodesic distance map $\mathcal{U}_{\mathfrak{s}}$ is chosen and tagged as *Accepted*. We set $\mathcal{L}(\mathbf{x}_{\min}) = k$ if $\mathbf{x}_{\min} \in \mathfrak{s}_k$. Otherwise, the geodesic distance value $\mathcal{U}_{\mathfrak{s}}(\mathbf{x}_{\min})$ can be estimated in the simplex $\mathbb{T}^* \in \mathcal{T}_{\mathbf{x}_{\min}}$ (see Eq. (11)), where the vertices relevant to \mathbb{T}^* are respective \mathbf{z}_1 and \mathbf{z}_2 . This is done by finding the solution to (13) with respect to the simplex \mathbb{T}^* , where the minimizer is $\boldsymbol{\lambda}^* = (\lambda_1^*, \lambda_2^*)$. Then the Voronoi index map \mathcal{L} can be computed by

$$\mathcal{L}(\mathbf{x}_{\min}) = \begin{cases} \mathcal{L}(\mathbf{z}_1), & \text{if } \lambda_1^* \geq \lambda_2^*, \\ \mathcal{L}(\mathbf{z}_2), & \text{otherwise.} \end{cases} \quad (14)$$

Local geodesic distance update. For a grid point \mathbf{x} , we denote by $\Lambda_{\star}(\mathbf{x}) := \{\mathbf{z} \in \mathbb{Z}^2; \mathbf{x} \in \Lambda(\mathbf{z})\}$ the reverse stencil. The remaining step in this iteration is to update $\mathcal{U}_{\mathfrak{s}}(\mathbf{z})$ for each grid point \mathbf{z} such that $\mathbf{z} \in \Lambda_{\star}(\mathbf{x}_{\min})$ and $b(\mathbf{z}) \neq \textit{Accepted}$ through the solution $\hat{\mathcal{U}}_{\mathfrak{s}}(\mathbf{z})$ to the Hopf-Lax operator (10). This is done by assigning to $\mathcal{U}_{\mathfrak{s}}(\mathbf{z})$ the smaller value between the solution $\hat{\mathcal{U}}_{\mathfrak{s}}(\mathbf{z})$ and the current geodesic distance value of $\mathcal{U}_{\mathfrak{s}}(\mathbf{z})$. Note that the solution $\hat{\mathcal{U}}_{\mathfrak{s}}(\mathbf{z})$ to (10) is attained using the stencil $\Lambda(\mathbf{z})$ [18]. The algorithm for the fast marching method is described in Algorithm 1. In this algorithm, the computation of a map $\mathfrak{C}_{\text{dyn}}$ in Line 12 of Algorithm 1 is not necessary for the general fast marching fronts propagation scheme, but required by our method as discussed in Section 4.2.

3 Finsler Metrics Construction

Definition 1. Let S_2^+ be the collection of all the positive definite symmetric matrices with size 2×2 . For any matrix $M \in S_2^+$, we define a norm $\|\mathbf{u}\|_M = \sqrt{\langle \mathbf{u}, M\mathbf{u} \rangle}$, $\forall \mathbf{u} \in \mathbb{R}^2$.

In this section, we present the construction method of the Finsler metric which is suitable for fronts propagation and image segmentation. Suppose that a vector field $\mathbf{g} : \Omega \rightarrow \mathbb{R}^2$ has been provided such that $\mathbf{g}(\mathbf{x})$ points to the object edges at least when \mathbf{x} is nearby them. In this case, the orthogonal vector field \mathbf{g}^{\perp} indicates the tangents of the edges.

¹ Initially, each source point $\mathbf{x} \in \mathfrak{s}$ is tagged as *Trial* and the remaining grid points are tagged as *Far*.

Algorithm 1 Fast Marching Fronts Propagation

Input: Source points set $\mathfrak{s} = \cup_k \mathfrak{s}_k$.
Output: Geodesic distance map $\mathcal{U}_{\mathfrak{s}}$ and Voronoi index map \mathcal{L} .

- 1: $\forall \mathbf{x} \in \Omega \setminus \mathfrak{s}$, set $\mathcal{U}_{\mathfrak{s}}(\mathbf{x}) \leftarrow \infty$ and $b(\mathbf{x}) \leftarrow \textit{Far}$.
- 2: $\forall \mathbf{x} \in \mathfrak{s}$, set $\mathcal{U}_{\mathfrak{s}}(\mathbf{x}) \leftarrow 0$ and $b(\mathbf{x}) \leftarrow \textit{Trial}$.
- 3: $\forall \mathbf{x} \in \mathfrak{s}_k$, set $\mathcal{L}(\mathbf{x}) = k$.
- 4: **while** there remains at least one *Trial* point **do**
- 5: Find a *Trial* point \mathbf{x}_{\min} globally minimizing $\mathcal{U}_{\mathfrak{s}}$.
- 6: Set $b(\mathbf{x}_{\min}) \leftarrow \textit{Accepted}$.
- 7: **if** $\mathbf{x}_{\min} \notin \mathfrak{s}$ **then**
- 8: Update the Voronoi index $\mathcal{L}(\mathbf{x}_{\min})$ by Eq. (14).
- 9: **end if**
- 10: **for** all $\mathbf{z} \in \mathbb{Z}^2$ such that $\mathbf{x}_{\min} \in \Lambda(\mathbf{z})$ **do**
- 11: **if** $b(\mathbf{z}) \neq \textit{Accepted}$ and $\mathbf{z} \notin \mathfrak{s}$ **then**
- 12: /* Update some map $\mathfrak{C}_{\text{dyn}}(\mathbf{z})$ if necessary. */
- 13: Find $\hat{\mathcal{U}}(\mathbf{z})$ by evaluating the Hopf-Lax formula (11).
- 14: Set $\mathcal{U}_{\mathfrak{s}}(\mathbf{z}) \leftarrow \min\{\mathcal{U}_{\mathfrak{s}}(\mathbf{z}), \hat{\mathcal{U}}(\mathbf{z})\}$ and $b(\mathbf{z}) \leftarrow \textit{Trial}$.
- 15: **end if**
- 16: **end for**
- 17: **end while**

Basically, the Eikonal equation-based fronts propagation models [9] perform the segmentation scheme through a geodesic distance map. In order to find a good solution for image segmentation, the used geodesic metric should be able to reduce the risk of front leaking problem. For this purpose, we search for a direction-dependent metric $\mathcal{F}_{\mathfrak{g}}$ satisfying the following inequality

$$\mathcal{F}_{\mathfrak{g}}(\mathbf{x}, \mathfrak{g}^{\perp}(\mathbf{x})) < \mathcal{F}_{\mathfrak{g}}(\mathbf{x}, \mathfrak{g}(\mathbf{x})) < \mathcal{F}_{\mathfrak{g}}(\mathbf{x}, -\mathfrak{g}(\mathbf{x})). \quad (15)$$

Recall that for an edge point \mathbf{x} , both the feature vectors $\mathfrak{g}^{\perp}(\mathbf{x})$ or $-\mathfrak{g}^{\perp}(\mathbf{x})$ are propositional to the tangent of the edge at \mathbf{x} . When the fast marching front arrives at the vicinity of image edges, it prefers to travel along the edge feature vectors $\mathfrak{g}^{\perp}(\mathbf{x})$ and $-\mathfrak{g}^{\perp}(\mathbf{x})$, instead of passing through the edges, i.e., prefers to travel along the direction $-\mathfrak{g}(\mathbf{x})$.

The inequality (15) requires the geodesic metric $\mathcal{F}_{\mathfrak{g}}$ to be anisotropic and asymmetric with respect to its second argument. Thus, we consider a Finsler metric with a Randers form [21] involving a symmetric quadratic term and a linear asymmetric term for any $\mathbf{x} \in \mathbb{R}^2$ and any vector $\mathbf{u} \in \mathbb{R}^2$

$$\mathcal{F}(\mathbf{x}, \mathbf{u}) := \mathfrak{C}(\mathbf{x}) \left(\|\mathbf{u}\|_{\mathcal{M}_{\mathfrak{g}}(\mathbf{x})} - \langle \boldsymbol{\omega}_{\mathfrak{g}}(\mathbf{x}), \mathbf{u} \rangle \right), \quad (16)$$

where $\mathcal{M}_{\mathfrak{g}} : \Omega \rightarrow S_2^+$ is a positive symmetric definite tensor field and $\boldsymbol{\omega}_{\mathfrak{g}} : \Omega \rightarrow \mathbb{R}^2$ is a vector field that is sufficiently small. The function $\mathfrak{C} : \Omega \rightarrow \mathbb{R}^+$ is a positive scalar-valued potential which gets small values in the homogeneous regions and large values around the image edges. It can be derived from the image data such as the coherence measurements of the image features, which will be discussed in detail in Section 4.2. The tensor field $\mathcal{M}_{\mathfrak{g}}$ and the vector

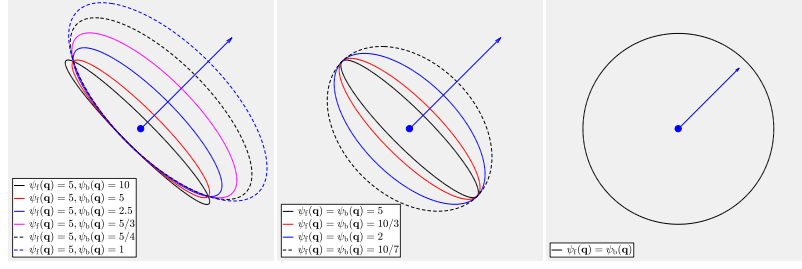


Fig. 2. Control sets for different metrics corresponding to different values of $\psi_f(\mathbf{x}_0)$ and $\psi_b(\mathbf{x}_0)$. The blue dots and the contours denote the origins and the boundaries of these balls, respectively.

field $\omega_{\mathbf{g}}$ should satisfy the constraint

$$\|\omega_{\mathbf{g}}(\mathbf{x})\|_{\mathcal{M}_{\mathbf{g}}^{-1}(\mathbf{x})} < 1, \forall \mathbf{x} \in \Omega, \quad (17)$$

in order to guarantee the positiveness [18] of the Randers metric \mathcal{F} .

We reformulate the Randers metric $\mathcal{F}_{\mathbf{g}}$ in Eq. (16) as

$$\mathcal{F}_{\mathbf{g}}(\mathbf{x}, \mathbf{u}) = \mathfrak{C}(\mathbf{x}) \mathcal{G}_{\mathbf{g}}(\mathbf{x}, \mathbf{u}), \quad (18)$$

where $\mathcal{G}_{\mathbf{g}} : \Omega \times \mathbb{R}^2 \rightarrow [0, \infty]$ is still a Randers metric formulated by

$$\mathcal{G}_{\mathbf{g}}(\mathbf{x}, \mathbf{u}) = \|\mathbf{u}\|_{\mathcal{M}_{\mathbf{g}}(\mathbf{x})} - \langle \omega_{\mathbf{g}}(\mathbf{x}), \mathbf{u} \rangle. \quad (19)$$

The remaining part of this section will be devoted to the construction of the Randers metric $\mathcal{G}_{\mathbf{g}}$ in terms of the vector field \mathbf{g} which is able to characterize the directions orthogonal to the image edges.

Let us define a new vector field $\bar{\mathbf{g}} : \Omega \rightarrow \mathbb{R}^2$ by $\bar{\mathbf{g}}(\mathbf{x}) := \mathbf{g}(\mathbf{x}) / \|\mathbf{g}(\mathbf{x})\|^2$. The tensor field $\mathcal{M}_{\mathbf{g}}$ used in Eq. (16) can be constructed dependently on two scalar-valued coefficient functions η_1 and η_2 such that

$$\mathcal{M}_{\mathbf{g}}(\mathbf{x}) = \eta_1^2(\mathbf{x}) \bar{\mathbf{g}}(\mathbf{x}) \otimes \bar{\mathbf{g}}(\mathbf{x}) + \eta_2(\mathbf{x}) \bar{\mathbf{g}}^\perp(\mathbf{x}) \otimes \bar{\mathbf{g}}^\perp(\mathbf{x}), \quad (20)$$

where $\bar{\mathbf{g}}^\perp(\mathbf{x})$ is the orthogonal vector of $\bar{\mathbf{g}}(\mathbf{x})$ and \otimes denotes the tensor product, i.e., $\mathbf{u} \otimes \mathbf{u} = \mathbf{u}\mathbf{u}^T$. Note that the eigenvalues of $\mathcal{M}_{\mathbf{g}}(\mathbf{x})$ are $\eta_1^2(\mathbf{x}) / \|\mathbf{g}(\mathbf{x})\|^2$ and $\eta_2(\mathbf{x}) / \|\mathbf{g}(\mathbf{x})\|^2$, respectively corresponding to the eigenvectors $\mathbf{g}(\mathbf{x}) / \|\mathbf{g}(\mathbf{x})\|$ and $\mathbf{g}^\perp(\mathbf{x}) / \|\mathbf{g}(\mathbf{x})\|$. The vector $\omega_{\mathbf{g}}(\mathbf{x})$ is positively collinear to field $\mathbf{g}(\mathbf{x})$ for all $\mathbf{x} \in \Omega$

$$\omega_{\mathbf{g}}(\mathbf{x}) = \tau(\mathbf{x}) \bar{\mathbf{g}}(\mathbf{x}), \quad (21)$$

where $\tau : \Omega \rightarrow \mathbb{R}$ is a scalar-valued coefficient function.

We estimate the coefficient functions η_1 , η_2 and τ through two cost functions $\psi_f, \psi_b : \Omega \rightarrow (1, +\infty)$, which assign the cost values $\psi_f(\mathbf{x})$, $\psi_b(\mathbf{x})$ and 1 to the Randers metric $\mathcal{G}_{\mathbf{g}}$ respectively along the directions $\mathbf{g}(\mathbf{x})$, $-\mathbf{g}(\mathbf{x})$ and $\mathbf{g}^\perp(\mathbf{x})$ for any point $\mathbf{x} \in \Omega$ such that

$$\mathcal{G}_{\mathbf{g}}(\mathbf{x}, \mathbf{g}(\mathbf{x})) = \psi_f(\mathbf{x}), \quad \mathcal{G}_{\mathbf{g}}(\mathbf{x}, -\mathbf{g}(\mathbf{x})) = \psi_b(\mathbf{x}), \quad \mathcal{G}_{\mathbf{g}}(\mathbf{x}, \mathbf{g}^\perp(\mathbf{x})) = 1. \quad (22)$$

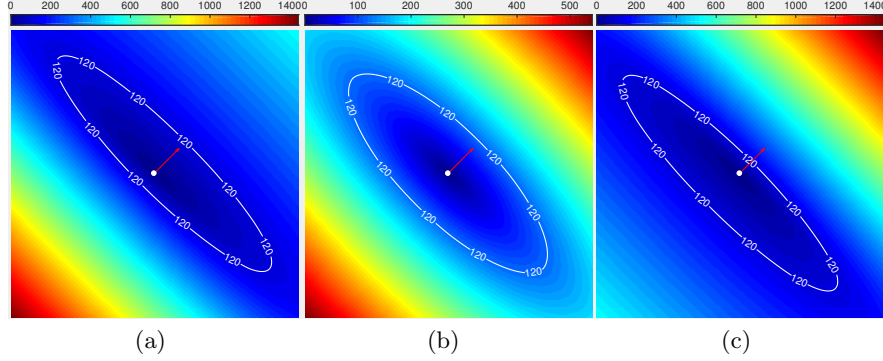


Fig. 3. Geodesic distance maps associated to the Randers metric $\mathcal{G}_{\mathbf{g}}$ with different values of ψ_f and ψ_b . The red arrow indicate the vector $(\cos(\pi/4), \sin(\pi/4))^T$. The white dots are the source points. Each white curve indicates a level set line of the respective geodesic distance map. (a) shows the geodesic distance map associated to $\psi_f \equiv 3$ and $\psi_b \equiv 8$. (b) shows the geodesic distance map associated to $\psi_f \equiv 3$ and $\psi_b \equiv 3$. (c) shows the geodesic distance map associated to $\psi_f \equiv 8$ and $\psi_b \equiv 3$.

Combining Eqs. (20) and (22) yields that

$$\eta_1(\mathbf{x}) - \tau(\mathbf{x}) = \psi_f(\mathbf{x}), \quad \eta_1(\mathbf{x}) + \tau(\mathbf{x}) = \psi_b(\mathbf{x}), \quad \eta_2(\mathbf{x}) = 1, \quad \forall \mathbf{x} \in \Omega. \quad (23)$$

The positive symmetric definite tensor field $\mathcal{M}_{\mathbf{g}}$ and the vector field $\boldsymbol{\omega}_{\mathbf{g}}$ thus can be respectively expressed in terms of the cost functions ψ_f and ψ_b by

$$\mathcal{M}_{\mathbf{g}}(\mathbf{x}) = \frac{1}{4}(\psi_f(\mathbf{x}) + \psi_b(\mathbf{x}))^2 \bar{\mathbf{g}}(\mathbf{x}) \otimes \bar{\mathbf{g}}(\mathbf{x}) + \bar{\mathbf{g}}^\perp(\mathbf{x}) \otimes \bar{\mathbf{g}}^\perp(\mathbf{x}), \quad (24)$$

$$\boldsymbol{\omega}_{\mathbf{g}}(\mathbf{x}) = \frac{1}{2}(\psi_b(\mathbf{x}) - \psi_f(\mathbf{x})) \bar{\mathbf{g}}(\mathbf{x}). \quad (25)$$

Based on the tensor field $\mathcal{M}_{\mathbf{g}}$ and the vector field $\boldsymbol{\omega}_{\mathbf{g}}$ respectively formulated in Eqs. (24) and (25), the positiveness constraint (17) is satisfied due to the assumption that $\psi_f(\mathbf{x}) > 1$ and $\psi_b(\mathbf{x}) > 1$, $\forall \mathbf{x} \in \Omega$. The cost functions ψ_f and ψ_b can be derived from the image edge information such as the image gradients, which will be discussed in Section 4.

Note that if we set $\psi_f \equiv \psi_b$, the vector field $\boldsymbol{\omega}_{\mathbf{g}}$ will vanish, i.e., $\boldsymbol{\omega}_{\mathbf{g}} \equiv \mathbf{0}$ (see Eq. (25)). In this case, one has $\langle \boldsymbol{\omega}_{\mathbf{g}}(\mathbf{x}), \mathbf{u} \rangle = 0$ for any point $\mathbf{x} \in \Omega$ and any vector $\mathbf{u} \in \mathbb{R}^2$, leading to a special form of the Randers metric $\mathcal{G}_{\mathbf{g}}$. This special form is a symmetric (potentially anisotropic) Riemannian metric $\mathcal{R}(\mathbf{x}, \mathbf{u}) = \|\mathbf{u}\|_{\mathcal{M}_{\mathbf{g}}(\mathbf{x})}$ which depends only on the tensor field $\mathcal{M}_{\mathbf{g}}$.

Tissots indicatrix. A basic tool for studying and visualizing the geometry distortion induced from a geodesic metric is the Tissots indicatrix defined as the collection of control sets in the tangent space [22]. For an arbitrary geodesic metric $\mathcal{F} : \Omega \times \mathbb{R}^2 \rightarrow [0, \infty]$, the control set $\mathcal{B}(\mathbf{x})$ for any point $\mathbf{x} \in \Omega$ is defined as the unit ball centered at \mathbf{x} such that $\mathcal{B}(\mathbf{x}) := \{\mathbf{u} \in \mathbb{R}^2; \mathcal{F}(\mathbf{x}, \mathbf{u}) \leq 1\}$. We

demonstrate the control sets $\mathcal{B}(\mathbf{q})$ in Fig. 2 for the Randers metric $\mathcal{G}_{\mathbf{g}}(\mathbf{q}, \cdot)$ with different values of $\psi_f(\mathbf{q})$ and $\psi_b(\mathbf{q})$ at a point $\mathbf{q} \in \Omega$. The vector $\mathbf{g}(\mathbf{q})$ is set as $\mathbf{g}(\mathbf{q}) = (\cos(\frac{\pi}{4}), \sin(\frac{\pi}{4}))^T$. In Fig. 2a, we show the control sets for the Randers metric $\mathcal{G}_{\mathbf{g}}$ with respect to different values of $\psi_b(\mathbf{q})$ and a fixed value $\psi_f(\mathbf{q}) = 5$. One can point out that the common origin of these control sets have shifted from the original center of the ellipses² due to the asymmetric property. In Fig. 2b, the control sets for the Randers metric $\mathcal{G}_{\mathbf{g}}$ associated to $\psi_f(\mathbf{q}) = \psi_b(\mathbf{q}) > 1$ are demonstrated, where $\mathcal{G}_{\mathbf{g}}(\mathbf{q}, \cdot)$ gets to be anisotropic and symmetric on its second argument. When $\psi_f(\mathbf{q}) = \psi_b(\mathbf{q}) = 1$, the values of the Randers metric $\mathcal{G}_{\mathbf{g}}(\mathbf{q}, \mathbf{u})$ turn to be invariant with respect to \mathbf{u} as shown in Fig. 2c. In this case, the tensor $\mathcal{M}_{\mathbf{g}}(\mathbf{q})$ is propositional to the identity matrix. In Fig. 3, we show the geodesic distance maps associated to $\mathcal{G}_{\mathbf{g}}$ with different values of the cost functions ψ_f and ψ_b . The vector field \mathbf{g} is set to $\mathbf{g} \equiv (\cos(\frac{\pi}{4}), \sin(\frac{\pi}{4}))^T$.

In Figs. 3a and 3c, we can see that the geodesic distance maps have strongly asymmetric and anisotropic appearance. In Fig. 3b, we observe that the geodesic distance map appears to be symmetric and strongly anisotropic. This is because the respective propagation speed of the fast marching fronts along the directions $(\cos(\pi/4), \sin(\pi/4))^T$ and $-(\cos(\pi/4), \sin(\pi/4))^T$ are identical to each other.

4 Numerical Considerations

Let $\mathbf{I} = (I_1, I_2, I_3) : \Omega \rightarrow \mathbb{R}^3$ be a vector-valued image in the chosen color space and let G_σ be a Gaussian kernel with variance σ (we set $\sigma = 1$ through all the experiments of this paper). The gradient of the image \mathbf{I} at each point $\mathbf{x} = (x, y)$ is a 2×3 Jacobian matrix $\nabla \mathbf{I}_\sigma(\mathbf{x}) = \nabla G_\sigma * \mathbf{I}(\mathbf{x})$ involving the Gaussian-smoothed first-order derivatives along the axis directions x and y

$$\nabla \mathbf{I}_\sigma(\mathbf{x}) = \begin{pmatrix} \partial_x G_\sigma * I_1 & \partial_x G_\sigma * I_2 & \partial_x G_\sigma * I_3 \\ \partial_y G_\sigma * I_1 & \partial_y G_\sigma * I_2 & \partial_y G_\sigma * I_3 \end{pmatrix}(\mathbf{x}). \quad (26)$$

Let $\rho : \Omega \rightarrow \mathbb{R}$ be an edge saliency map. It has high values in the vicinity of image edges and low values inside the flatten regions. For each domain point $\mathbf{x} \in \Omega$, the value of $\rho(\mathbf{x})$ can be computed by the Frobenius norm of the Jacobian matrix $\nabla \mathbf{I}_\sigma(\mathbf{x})$

$$\rho(\mathbf{x}) = \sqrt{\sum_{i=1}^3 (|\partial_x G_\sigma * I_i(\mathbf{x})|^2 + |\partial_y G_\sigma * I_i(\mathbf{x})|^2)}. \quad (27)$$

For a gray level image $I : \Omega \rightarrow \mathbb{R}$, the edge saliency map ρ can be simply computed by the norm of the Euclidean gradient of the image I such that

$$\rho(\mathbf{x}) = \sqrt{|\partial_x G_\sigma * I(\mathbf{x})|^2 + |\partial_y G_\sigma * I(\mathbf{x})|^2}. \quad (28)$$

² These ellipses are the boundaries of the control sets.

4.1 Construction of the vector field \mathbf{g}

We use the gradient vector flow method [23] to compute the vector field \mathbf{g} for the construction of the Randers metric $\mathcal{F}_{\mathbf{g}}$. This can be done by minimizing the following functional \mathcal{E}_{gvf} with respect to a vector field $\mathbf{h} = (h_1, h_2)^T : \Omega \rightarrow \mathbb{R}^2$, where \mathcal{E}_{gvf} can be expressed as

$$\mathcal{E}_{\text{gvf}}(\mathbf{h}) = \epsilon \mathcal{E}_{\text{reg}}(\mathbf{h}) + \mathcal{E}_{\text{data}}(\mathbf{h}), \quad (29)$$

where $\epsilon \in \mathbb{R}^+$ is a constant and

$$\mathcal{E}_{\text{reg}}(\mathbf{h}) = \int_{\Omega} (\|\nabla h_1(\mathbf{x})\|^2 + \|\nabla h_2(\mathbf{x})\|^2) d\mathbf{x}, \quad (30)$$

$$\mathcal{E}_{\text{data}}(\mathbf{h}) = \int_{\Omega} \|\nabla \rho(\mathbf{x})\|^2 \|\mathbf{h}(\mathbf{x}) - \nabla \rho(\mathbf{x})\|^2 d\mathbf{x}. \quad (31)$$

The parameter ϵ controls the balance between the regularization term \mathcal{E}_{reg} and the data fidelity term $\mathcal{E}_{\text{data}}$. As discussed in [23], the values of ϵ should depend on the image noise levels such that a large value of ϵ is able to suppress the effects from image noise. We set $\epsilon = 0.1$ through all the numerical experiments of this paper. The minimization of the functional \mathcal{E}_{gvf} can be carried out by solving the Euler-Lagrange equations of the functional \mathcal{E}_{gvf} with respect to the components h_1 and h_2 . The gradient vector flow \mathbf{h} is more dense and smooth than the original gradient field $\nabla \rho$. The vector field \mathbf{g} for the construction of the Randers metric $\mathcal{G}_{\mathbf{g}}$ can be obtained by normalizing the vector field \mathbf{h}

$$\mathbf{g}(\mathbf{x}) = \mathbf{h}(\mathbf{x}) / \|\mathbf{h}(\mathbf{x})\|, \quad \forall \mathbf{x} \in \Omega. \quad (32)$$

The cost functions ψ_f and ψ_b used in Eq. (22) for the foreground and background segmentation application can be expressed for any $\mathbf{x} \in \Omega$ by

$$\psi_f(\mathbf{x}) = \exp(\alpha_f \rho(\mathbf{x}) / \|\rho\|_{\infty}), \quad \psi_b(\mathbf{x}) = \exp(\alpha_b \rho(\mathbf{x}) / \|\rho\|_{\infty}) \psi_f(\mathbf{x}), \quad (33)$$

where α_f and α_b are non-negative constants dominating how anisotropic and asymmetric the Randers metric $\mathcal{G}_{\mathbf{g}}$ is. Once the cost functions ψ_f and ψ_b have been computed by Eq. (33), we can construct the tensor field $\mathcal{M}_{\mathbf{g}}$ and the vector field $\omega_{\mathbf{g}}$ respectively via Eqs. (24) and (25). Indeed, one has $\psi_f(\mathbf{x}) \approx \psi_b(\mathbf{x}) \approx 1$ for the points \mathbf{x} located in the homogeneous region of the image \mathbf{I} where $\rho(\mathbf{x}) \approx 0$. In this case, the data-driven Randers metric $\mathcal{G}_{\mathbf{g}}(\mathbf{x}, \cdot)$ in Eq. (19) approximates to be an isotropic Riemannian metric. For each point \mathbf{x} around the image edges where the value of $\rho(\mathbf{x})$ is large, the Randers metric $\mathcal{G}_{\mathbf{g}}(\mathbf{x}, \cdot)$ will appear to be strongly anisotropic and asymmetric.

4.2 Computing the Potential \mathfrak{C}

We present the computation methods for the potential function \mathfrak{C} used by the data-driven Randers metric in Eq. (18). Basically, the function \mathfrak{C} should have

small values in the flatten regions and large values in the vicinity of image edges. The potential function \mathfrak{C} can be expressed by

$$\mathfrak{C}(\mathbf{x}) = \exp(\beta_s \rho(\mathbf{x}) / \|\rho\|_\infty) \mathfrak{C}_{\text{dyn}}(\mathbf{x}), \quad (34)$$

where β_s is a positive constant and ρ is the edge saliency map defined in Eqs. (27) or (28). The term $\exp(\beta_s \rho(\mathbf{x}))$ which depends only on the edge saliency map ρ will keep invariant during the fast marching fronts propagation. The dynamic potential function $\mathfrak{C}_{\text{dyn}}$ relies on the positions of the fronts. It will be updated in the course of the geodesic distances computation in terms of some consistency measure of image features [14]. Basically, the values of the dynamic potential $\mathfrak{C}_{\text{dyn}}$ should be small in the homogeneous regions. We use a feature map $\mathfrak{F} : \Omega \rightarrow \mathbb{R}^n$ with n the dimensions of the feature vector to establish the dynamic potential $\mathfrak{C}_{\text{dyn}}$. The feature map \mathfrak{F} can be the image color vector ($n = 3$), the image gray level ($n = 1$), or the scalar probability map ($n = 1$) as used in [14].

Recall that in each fast marching distance update iteration, the latest *Accepted* point \mathbf{x}_{\min} is chosen by searching for a *Trial* point with minimal distance value \mathcal{U}_s (\mathfrak{s} is the set of the source points), i.e.,

$$\mathbf{x}_{\min} := \arg \min_{\mathbf{x}:b(\mathbf{x})=\text{Trial}} \mathcal{U}_s(\mathbf{x}). \quad (35)$$

Then the value of $\mathfrak{C}_{\text{dyn}}(\mathbf{z})$ for each point $\mathbf{z} \in \mathbb{Z}^2 \setminus \mathfrak{s}$ such that $\mathbf{x}_{\min} \in \Lambda(\mathbf{z})$ and $b(\mathbf{z}) \neq \text{Accepted}$ can be updated by evaluating the Euclidean distance between $\mathfrak{F}(\mathbf{z})$ and $\mathfrak{F}(\mathbf{x}_{\min})$ (see Line 12 of Algorithm 1). In other words, one can compute the dynamic potential $\mathfrak{C}_{\text{dyn}}$ in each fast marching update iteration by

$$\mathfrak{C}_{\text{dyn}}(\mathbf{z}) = \exp(\beta_d \|\mathfrak{F}(\mathbf{z}) - \mathfrak{F}(\mathbf{x}_{\min})\|) \quad (36)$$

for all grid points $\mathbf{z} \in \mathbb{Z}^2 \setminus \mathfrak{s}$ such that $\mathbf{x}_{\min} \in \Lambda(\mathbf{z})$ and $b(\mathbf{z}) \neq \text{Accepted}$, where β_d is a positive constant. Note that we initialize the dynamic potential $\mathfrak{C}_{\text{dyn}}$ by $\mathfrak{C}_{\text{dyn}}(\mathbf{x}) = 1, \quad \forall \mathbf{x} \in \mathfrak{s}$.

5 Experimental Results

The anisotropy and asymmetry of the Randers metric \mathcal{G}_g is determined by the parameters α_f and α_b (see Eq. (33)). We denote by \mathcal{G}_g^α the Randers metric \mathcal{G}_g with a pair of parameters $\alpha = (\alpha_f, \alpha_b)$. In this case, the corresponding Randers metric \mathcal{F}_g in Eq. (18) can be noted by \mathcal{F}_g^α . The potential function \mathfrak{C} relies on two parameters β_s and β_d . We fix $\beta_d = 10$ through all the experiments, except in Fig. 5 for which we set $\beta_d = 5$. The values of β_s are individually set for each experiment. Note that the parameter $\alpha = (0, 0)$ means that the metric $\mathcal{G}_g^{(0,0)}$ is isotropic with respect to its second argument. Furthermore, when $\alpha = (a, 0)$ with $a \in \mathbb{R}^+$, the metric $\mathcal{G}_g^{(a,0)}$ gets to be the anisotropic Riemannian cases³.

³ Note that metric \mathcal{G}_g^α has the identical anisotropy and asymmetry properties to \mathcal{F}_g^α .

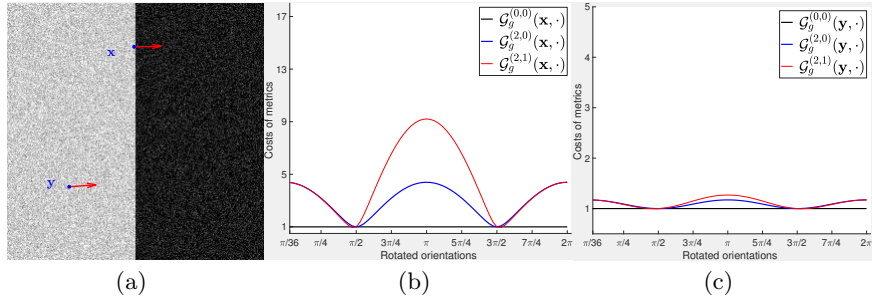


Fig. 4. (a) shows a synthetic image. The blue dots indicate two sampled points. The arrows indicate the directions $\mathbf{g}(\mathbf{x})$ and $\mathbf{g}(\mathbf{y})$. (b) and (c) respectively plot the cost values of $\mathcal{G}_g^{(0,0)}$, $\mathcal{G}_g^{(2,0)}$ and $\mathcal{G}_g^{(2,1)}$ at points \mathbf{x} and \mathbf{y} along different directions.

The interactive foreground and background segmentation task can be converted to the problem of identifying the Voronoi index map or Voronoi regions in terms of geodesic distance [13, 14]. Let \mathfrak{s}_1 and \mathfrak{s}_2 be the sets of source points which are respectively located at the foreground and background regions. The Voronoi regions \mathcal{V}_1 and \mathcal{V}_2 , indicating foreground and background regions respectively, can be determined by the Voronoi index map \mathcal{L} through Eq. (8) such that $\mathcal{V}_i := \{\mathbf{x} \in \Omega; \mathcal{L}(\mathbf{x}) = i\}$, $i = 1, 2$.

Let us consider a synthetic image as shown in Fig. 4a with two sampled points \mathbf{x} and \mathbf{y} indicated by blue dots. The arrows respectively indicate the directions of $\mathbf{g}(\mathbf{x})$ and $\mathbf{g}(\mathbf{y})$, where \mathbf{x} is near the edges and \mathbf{y} is located inside the homogeneous region. In Fig. 4b, we plot the cost values of the metrics $\mathcal{G}_g^{(0,0)}(\mathbf{x}, \mathbf{u}_j)$, $\mathcal{G}_g^{(2,0)}(\mathbf{x}, \mathbf{u}_j)$ and $\mathcal{G}_g^{(2,1)}(\mathbf{x}, \mathbf{u}_j)$, along different directions $\mathbf{u}_j \in \mathbb{R}^2$. The directions \mathbf{u}_j are obtained by rotation such that $\mathbf{u}_j = M(j\theta_s)\mathbf{g}(\mathbf{x})$, $j = 1, 2, \dots, 72$, where $\theta_s = \pi/36$ is the angle resolution and $M(j\theta_s)$ is a rotation matrix with angle $j\theta_s$ in a count-clockwise order. In Fig. 4c, we plot the cost values for the metrics $\mathcal{G}_g^{(0,0)}(\mathbf{y}, \mathbf{v}_j)$, $\mathcal{G}_g^{(2,0)}(\mathbf{y}, \mathbf{v}_j)$ and $\mathcal{G}_g^{(2,1)}(\mathbf{y}, \mathbf{v}_j)$ with $\mathbf{v}_j = M(j\theta_s)\mathbf{g}(\mathbf{y})$. In Fig. 4b, we can see that all of the three metrics get low values around the directions $M(\pi/2)\mathbf{g}(\mathbf{x})$ and $M(3\pi/2)\mathbf{g}(\mathbf{x})$, which are orthogonal to the direction $\mathbf{g}(\mathbf{x})$. However, around the direction $-\mathbf{g}(\mathbf{x})$, the Randers metric $\mathcal{G}_g^{(2,1)}$ attains much larger values than the Riemannian cases $\mathcal{G}_g^{(0,0)}$ and $\mathcal{G}_g^{(2,0)}$. Such an asymmetric property is able to reduce the risk of front leakages.

In Fig. 5, we show the fronts propagation results on a synthetic image. In the first column of Fig. 5, we initialize the sets of the source points in different locations, which are indicated by green and blue brushes. The columns 2 to 4 of Fig. 5 are the segmentation results from the isotropic Riemannian metric $\mathcal{F}_g^{(0,0)}$, the anisotropic Riemannian metric $\mathcal{F}_g^{(2,0)}$ and the Randers metric $\mathcal{F}_g^{(2,3)}$, respectively. For the purpose of fair comparisons, the three metrics used in this experiment share the same potential function \mathfrak{C} defined in Eq. (34). One can point out that the results from the metrics $\mathcal{F}_g^{(0,0)}$ and $\mathcal{F}_g^{(2,0)}$ suffer from the

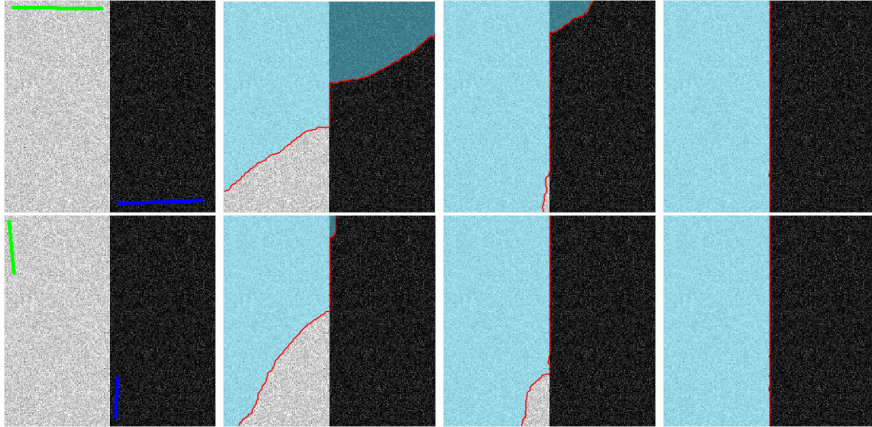


Fig. 5. Image segmentation via different geodesic metrics on a synthetic image. **Column 1** shows the initializations, where the green and blue brushes indicating the seeds in different regions. **Columns 2-4** show the segmentation results by the fronts propagation associated to the isotropic Riemannian metric $\mathcal{F}_g^{(0,0)}$, the anisotropic Riemannian metric $\mathcal{F}_g^{(2,0)}$ and the Randers metric $\mathcal{F}_g^{(2,3)}$, respectively.

leaking problem, while the final boundaries (red curves) associated the proposed Randers metric $\mathcal{F}_g^{(2,3)}$ are able to catch the expected edges thanks to the asymmetric enhancement. In this experiment, we choose $\beta_d = 5$.

In Fig. 6, we compare the interactive image segmentation results via different geodesic metrics on real images [24, 25]. The final segmentation results are derived from the boundaries of the corresponding Voronoi index maps. In column 1, we show the initial images with seeds indicating by green and blue brushes respectively inside the foreground and background regions. In columns 2 to 4 of Fig. 6, we demonstrate the segmentation results obtained via the isotropic Riemannian metric $\mathcal{F}_g^{(0,0)}$, the anisotropic Riemannian metric $\mathcal{F}_g^{(2,0)}$ and the Randers Metric $\mathcal{F}_g^{(2,3)}$. For the results from the isotropic and anisotropic Riemannian metrics (shown in columns 2 and 3), the final contours leak into the background regions. In contrast, the segmentation contours associated to the Randers metric $\mathcal{F}_g^{(2,3)}$ are able to follow the desired object boundaries.

6 Conclusion

In this paper, we extend the fronts propagation framework from the Riemannian case to a general Finsler case with applications to image segmentation. The Finsler metric with a Randers form allows us to take into account the asymmetric and anisotropic image features in order to reduce the risk of the leaking problem during the fronts propagation. We presented a method for the construction of the Finsler metric with a Randers form using a vector field derived from the image edges. This metric can also integrate with a feature coherence

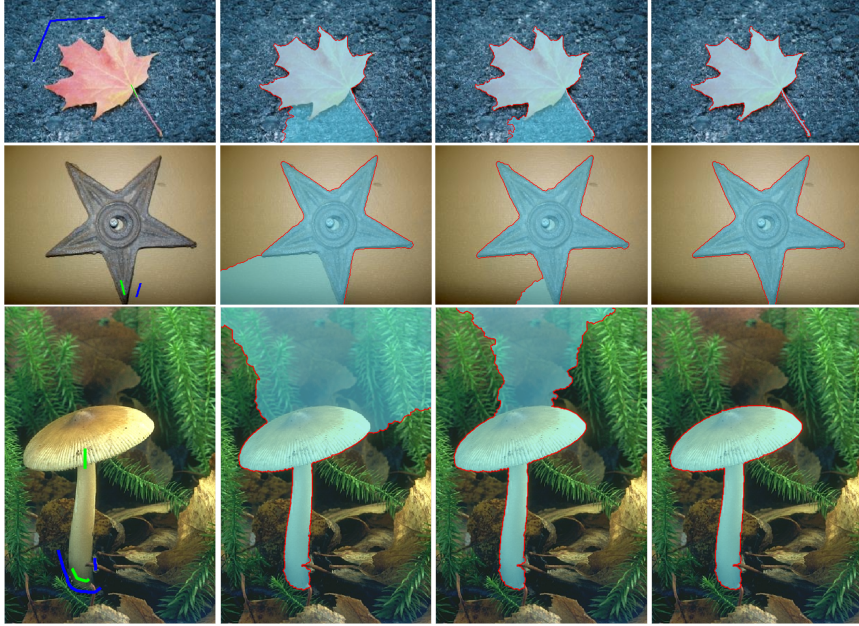


Fig. 6. Image segmentation via different geodesic metrics on real images. **Column 1** shows the initializations, where the green and blue brushes are the seeds for background and foreground regions. **Columns 2-4** show the segmentation results by the metrics $\mathcal{F}_g^{(0,0)}$, $\mathcal{F}_g^{(2,0)}$ and $\mathcal{F}_g^{(2,3)}$, respectively.

penalization term updated in the course of the fast marching fronts propagation. Experimental results show that the proposed model indeed produces promising image segmentation results.

Acknowledgment

The authors would like to thank all the anonymous reviewers for their detailed remarks that helped us improve the presentation of this paper. The authors thank Dr. Jean-Marie Mirebeau from Université Paris-Sud for his fruitful discussion and creative suggestions. The first author also thanks Dr. Gabriel Peyré from ENS Paris for his financial support. This work was partially supported by the European Research Council (ERC project SIGMA-Vision).

References

1. Osher, S., Sethian, J.A.: Fronts propagating with curvature-dependent speed: algorithms based on Hamilton-Jacobi formulations. *JCP* **79**(1) (1988) 12–49
2. Caselles, V., Catté, F., Coll, T., Dibos, F.: A geometric model for active contours in image processing. *Numerische Mathematik* **66**(1) (1993) 1–31

3. Malladi, R., Sethian, J., Vemuri, B.C.: Shape modeling with front propagation: A level set approach. *TPAMI* **17**(2) (1995) 158–175
4. Caselles, V., Kimmel, R., Sapiro, G.: Geodesic active contours. *IJCV* **22**(1) (1997) 61–79
5. Yezzi, A., Kichenassamy, S., Kumar, A., Olver, P., Tannenbaum, A.: A geometric snake model for segmentation of medical imagery. *TMI* **16**(2) (1997) 199–209
6. Kass, M., Witkin, A., Terzopoulos, D.: Snakes: Active contour models. *IJCV* **1**(4) (1988) 321–331
7. Adalsteinsson, D., Sethian, J.A.: A fast level set method for propagating interfaces. *JCP* **118**(2) (1995) 269–277
8. Li, C., Xu, C., Gui, C., Fox, M.D.: Distance regularized level set evolution and its application to image segmentation. *TIP* **19**(12) (2010) 3243–3254
9. Malladi, R., Sethian, J.A.: A real-time algorithm for medical shape recovery. In: *Proceeding of ICCV*. (1998) 304–310
10. Sethian, J.A.: Fast marching methods. *SIAM Review* **41**(2) (1999) 199–235
11. Tsitsiklis, J.N.: Efficient algorithms for globally optimal trajectories. *TAC* **40**(9) (1995) 1528–1538
12. Chen, D., Cohen, L.D.: Vessel tree segmentation via front propagation and dynamic anisotropic riemannian metric. In: *Proceedings of ISBI*. (2016) 1131–1134
13. Arbeláez, P.A., Cohen, L.D.: Energy partitions and image segmentation. *JMIV* **20**(1) (2004) 43–57
14. Bai, X., Sapiro, G.: Geodesic matting: A framework for fast interactive image and video segmentation and matting. *IJCV* **82**(2) (2009) 113–132
15. Li, H., Yezzi, A.: Local or global minima: Flexible dual-front active contours. *TPAMI* **29**(1) (2007)
16. Cohen, L.D., Deschamps, T.: Segmentation of 3D tubular objects with adaptive front propagation and minimal tree extraction for 3D medical imaging. *CMBBE* **10**(4) (2007) 289–305
17. Melonakos, J., Pichon, E., Angenent, S., Tannenbaum, A.: Finsler active contours. *TPAMI* **30**(3) (2008) 412–423
18. Mirebeau, J.M.: Efficient fast marching with Finsler metrics. *Numerische Mathematik* **126**(3) (2014) 515–557
19. Benmansour, F., Cohen, L.D.: Fast object segmentation by growing minimal paths from a single point on 2d or 3d images. *JMIV* **33**(2) (2009) 209–221
20. Cohen, L.: Multiple contour finding and perceptual grouping using minimal paths. *JMIV* **14**(3) (2001) 225–236
21. Randers, G.: On an asymmetrical metric in the four-space of general relativity. *Physical Review* **59**(2) (1941) 195
22. Chen, D., Mirebeau, J.M., Cohen, L.D.: Global minimum for a Finsler elastica minimal path approach. *IJCV* **122**(3) (2017) 458–483
23. Xu, C., Prince, J.L.: Snakes, shapes, and gradient vector flow. *TIP* **7**(3) (1998) 359–369
24. Alpert, S., Galun, M., Brandt, A., Basri, R.: Image segmentation by probabilistic bottom-up aggregation and cue integration. *TPAMI* **34**(2) (2012) 315–327
25. Rother, C., Kolmogorov, V., Blake, A.: Grabcut: Interactive foreground extraction using iterated graph cuts. *ToG* **23**(3) (2004) 309–314